

# Understanding the spatial variation of Mg II and ionizing photon escape in a local LyC leaker

Thomas Seive,<sup>1</sup>★ John Chisholm,<sup>1</sup> Floriane Leclercq,<sup>1</sup> Gregory Zeimann,<sup>1</sup>

<sup>1</sup>*Department of Astronomy, University of Texas, Austin, TX 78712, USA*

Accepted XXX. Received YYY; in original form ZZZ

## ABSTRACT

Ionizing photons must have escaped from high-redshift galaxies, but the neutral high-redshift intergalactic medium makes it unlikely to directly detect the escape of ionizing photons during the epoch of reionization. Indirect methods of studying ionizing photon escape fractions present a way to infer escape fractions and understand how ionizing photons escape from the first galaxies. Here, we use HET/LRS2 observations of J0919+4906, a confirmed  $z \approx 0.4$  emitter of ionizing photons, to achieve spatially resolved spectroscopy of Mg II  $\lambda 2796$ , Mg II  $\lambda 2803$ , [O II]  $\lambda 3728$ , [Ne III]  $\lambda 3869$ , H $\gamma$ , [O III]  $\lambda 4363$ , H $\beta$ , [O III]  $\lambda 4959$ , and [O III]  $\lambda 5007$ . From these data we measure Mg II emission, which is a promising indirect tracer of ionizing photons, along with nebular ionization and dust attenuation in multiple spatially-resolved apertures. We find that J0919+4906 has significant spatial variation in its Mg II escape and thus ionizing photon escape fraction. Combining our observations with photoionization models, the regions with the largest relative Mg II emission and Mg II escape fractions have the highest ionization and lowest dust attenuation. Some regions have nearly unity escape fraction, while other regions transmit very little ( $\sim 10\%$ ) of their intrinsic Mg II emission. Dust absorbs more Lyman Continuum photons than Mg II photons such that regions with high attenuation and low Mg II escape have even lower Lyman Continuum escape fractions. There is substantial scatter in the Mg II escape fraction of individual sightlines, but the average of all sightlines is similar to the integrated Mg II escape fraction. For example, the integrated aperture has an order of magnitude fewer ionizing photon escape than the central aperture. This makes the integrated escape fraction lower than the value typically quoted as being sufficient to reionize the universe, even though the central value is higher. Our results suggest that single sightline observations may not trace the volume-averaged escape fraction of ionizing photons which may introduce significant scatter into the indirect tracers of ionizing photon escape.

**Key words:** keyword1 – keyword2 – keyword3

## 1 INTRODUCTION

Between redshifts of 5–10, the intergalactic medium in the early universe rapidly went through a phase transition from neutral to ionized (Becker et al. 2001; Fan et al. 2006; Bañados et al. 2017; Becker et al. 2021). This ionization was brought about by Lyman Continuum (LyC) photons which have  $\lambda < 912 \text{ \AA}$ . Understanding the source of these photons will reveal the timing, duration, and overall evolution of large scale structure in the universe (Robertson et al. 2013; Madau & Dickinson 2014; Robertson et al. 2015). Furthermore, the process of understanding the sources of ionizing photons can inform us about the quenching of dwarf galaxies in the early universe (Bullock et al. 2000) and why the intergalactic medium is the temperature that it is (Miralda-Escudé & Rees 1994). Thus, understanding ionizing photons has far reaching consequences for establishing the observable universe.

Initially, the debate around the sources of reionization centered around whether active galactic nuclei (AGN) or massive stars were most responsible for providing ionizing photons (Oesch et al. 2009; Faucher-Giguère et al. 2009; Robertson et al. 2013; Madau & Haardt

2015). AGN generate many ionizing photons and are concentrated in the depths of gravitational potentials. However, current observations find that there are too few AGNs to reionize the universe (Hopkins et al. 2008; Onoue et al. 2017; Ricci et al. 2016; Matsuoka et al. 2018; Shen et al. 2020). On the other hand, star forming galaxies are readily observed at the required redshifts and are broadly distributed spatially. In order to be star forming, they must have large amounts of cold gas. This cold, neutral gas will efficiently absorb ionizing photons, nearly eliminating the photons that escape a typical star-forming galaxy. This reduction in escape fraction of star forming galaxies has shifted the current debate to whether widely distributed low-mass galaxies or heavily clustered bright massive galaxies were the sources of ionizing photons (Finkelstein et al. 2019; Naidu et al. 2020; Matthee et al. 2021). The difference in concentration between the various types of ionizing photon sources will affect the morphology of reionization. Infrequent, concentrated sources (e.g. AGNs and massive galaxies) will yield a much patchier evolution of reionization when compared to the less powerful and more evenly distributed sources (e.g. low-mass galaxies) (sources needed). The morphology of reionization has ramifications for the kinds of structures the Universe forms.

The number density of ionizing photons that escape a source,

★ E-mail: thomasseive@utexas.edu

known as the emissivity ( $J_{\text{ion}}$  [photon  $\text{s}^{-1} \text{Mpc}^{-3}$ ]), requires measurements of the density of sources and the production of ionizing photons of each source.  $J_{\text{ion}}$  can be numerically represented as

$$J_{\text{ion}} = f_{\text{esc}}(\text{LyC}) \xi_{\text{ion}} \rho_{\text{UV}} \quad (1)$$

where  $f_{\text{esc}}(\text{LyC})$  is the fraction of ionizing photons that escape from all directions of a galaxy,  $\xi_{\text{ion}}$  is the intrinsic production of ionizing photons per far ultraviolet (FUV) luminosity for each source, and  $\rho_{\text{UV}}$  is the FUV luminosity function. Observing all of these parameters for star forming galaxies in the Epoch of Reionization (EOR) would answer how the Universe became ionized. Unfortunately, all of these parameters have their own challenges associated with measuring them, with escape fractions currently being the most uncertain of them.

Confirming whether star forming galaxies emitted a sufficient number of ionizing photons to reionize the Universe requires observations of the LyC escape fraction. However, observing LyC escape fractions at redshifts between  $z \approx 4$  and the EoR would be difficult because of intervening neutral gas. Recently, there has been tremendous success with directly measuring the escape of ionizing photons at low-redshift, with measurements of escape fractions between 0-70% (Grimes et al. 2009; Vanzella et al. 2010; Leitert, E. et al. 2011; Borthakur et al. 2014; Izotov et al. 2016a,b; Leitherer et al. 2016; Shapley et al. 2016; Vanzella et al. 2016; Izotov et al. 2017, 2018; Naidu et al. 2018; Steidel et al. 2018; Fletcher et al. 2019; Rivera-Thorsen et al. 2019; Wang et al. 2019; Izotov et al. 2021). Recently, indirect tracers of LyC escape have proven to be a promising route to penetrate the barriers at the EoR. Thus far, these methods have included Ly $\alpha$  emission properties (Verhamme et al. 2015; Rivera-Thorsen et al. 2017; Izotov et al. 2018; Gazagnes et al. 2021; Izotov et al. 2021), ISM absorption properties (Reddy et al. 2016; Gazagnes et al. 2018; Chisholm et al. 2018; Steidel et al. 2018), resonant emission lines (Henry et al. 2018; Chisholm et al. 2020; Witstok et al. 2021), and optical emission line ratios (Nakajima & Ouchi 2014; Oey et al. 2014; Wang et al. 2019). Of all of these tracers, the resonant line Mg II has shown great promise as a tracer of LyC escape (Henry et al. 2018; Chisholm et al. 2020). Due to being a resonant line, emission from the Mg II doublet has been found to trace neutral gas column densities less than  $10^{17} \text{cm}^{-2}$  (Chisholm et al. 2020). This makes it capable of determining a neutral gas column density low enough to transmit ionizing photons. Along with this, the ionization energy of Mg II overlaps with that of neutral hydrogen (15 eV vs 13.6 eV, respectively). For all these reasons, Mg II emission has been suggested to be an ideal indirect indicator of the escape of ionizing photons.

All of these methods have had major work to either directly measure escape fractions or use observations to stringently test indirect methods. However, indirect or direct, all the previously mentioned measurements have all been along single sightlines. These single sightlines are one out of a nearly infinite amount of ways to observe the galaxy. As mentioned above, an understanding of reionization requires the total amount of ionizing photons that escape from all sides of a galaxy and reach the intergalactic medium, also known as a volume averaged escape fraction. Without a volume averaged escape fraction, it is challenging to extrapolate single sightline LyC measurements to observations of the EoR. From this challenge, a series of questions naturally arise: How can we interpret a single sightline LyC observation? Does this single sightline observation relate to the volume averaged escape fraction? Does spatial variation obscure the picture created by single sightline observations?

Here we aim to answer these questions and test the spatial variation of the neutral gas opacity in a previously confirmed  $z \approx 0.4$ , LyC

emitting galaxy (Izotov et al. 2021). We use spatially resolved IFU observations from the Low Resolution Spectrograph 2 (LRS2) instrument on the Hobby-Eberly Telescope (HET), to determine Mg II and other emission lines to test if spatial variation in Mg II flux, dust, and ionization in a target can lead to substantial variation in sightline to sightline escape fractions. In section 2 we describe the LRS2 observations and data reduction. section 3 describes our process for extracting emission line parameters and draws similarities and differences to other observations of this galaxy in the literature. Our observations of the dust, ionization, and Mg II emission are described in section 4. We conclude in section 5 by exploring the implications of our measurements for single sightline observations. Throughout the paper, all distances are in physical units, not comoving. We assume a flat  $\Lambda$ CDM cosmology with  $m = 0.315$  and  $H_0 = 67.4 \text{ km s}^{-1} \text{Mpc}^{-1}$  (Planck Collaboration et al. 2021); in this framework, a 1" angular separation corresponds to 5 kpc proper at the redshift of the galaxy.

## 2 OBSERVATIONS AND REDUCTIONS

### 2.1 Observations

We observed J0919+4906 (RA: 09:19:55.78, Dec: +49:06:08.75) over 3 nights (January 8th 2021, January 9th 2021, and March 3rd 2021) with four total exposures using the LRS2 spectrograph (Chonis et al. 2014) on the Hobby-Eberly Telescope. Three of the exposures had an exposure time of 1800 seconds using the LRS2-B configuration. The fourth exposure had an exposure time of 500 seconds with the LRS2-R configuration. This object is of interest because it was one of the recently discovered Lyman Continuum (LyC) emitters from Izotov et al. (2021). The maximum seeing was  $\approx 2.6''$  and the spatial scale of the observations was  $0.25''$  by  $0.25''$  per spaxel. The spectral resolution of the observation depends on the LRS2 spectrograph arm (UV:  $1.63 \text{\AA}$ , Orange:  $4.44 \text{\AA}$ , Red:  $3.03 \text{\AA}$ , Farred:  $3.78 \text{\AA}$ ).

This object has been observed with the SDSS in the optical (Aguado et al. 2019) and HST/COS in the FUV (Izotov et al. 2021). These observations supplement our work. The SDSS observation provides values to compare against the LRS2 observations (subsection 3.4). From our central aperture (Figure 1), we measure a Signal to Noise Ratio (SNR) of 70 in [O II] $\lambda 3728$ , which is one of our weakest emission lines. This SNR is  $\sim 2$  times higher than the SNR of 38 from the SDSS for the same line. The HST/COS observations provide a direct measurement of 16% for the LyC escape fraction (Izotov et al. 2021). The LyC escape fraction is a value we attempt to indirectly measure in this work (subsection 5.1).

### 2.2 Data reduction

The HET observations reported here were obtained with the LRS2 spectrograph. LRS2 comprises two spectrographs separated by 100 arcseconds on sky: LRS2-B (with wavelength coverage of  $3650 \text{\AA} - 6950 \text{\AA}$ ) and LRS2-R (with wavelength coverage of  $6450 \text{\AA} - 10500 \text{\AA}$ ). Each spectrograph has 280 fibers covering  $6 \times 12$  with nearly unity fill factor (Chonis et al. 2014). We used the HET LRS2 pipeline, Panacea<sup>1</sup>, to perform the initial reductions including: fiber extraction, wavelength calibration, astrometry, and flux calibration. There are two channels for each spectrograph: UV and Orange for LRS2-B and Red and Farred for LRS2-R. On each exposure, we

<sup>1</sup> <https://github.com/grzeimann/Panacea>

combined fiber spectra from the two channels into a single data cube accounting for differential atmospheric refraction. We then identified the target galaxy in each observation and rectified the data cubes to a common sky coordinate grid with target at the center.

We first smoothed each cube to the worst seeing conditions of the four observations using a Gaussian model. To normalize each cube, we measured  $H\beta$  in both LRS2-B and LRS2-R at the observed wavelength of  $\approx 6831\text{\AA}$ . After normalization we stacked the individual cubes together using a variance weighted mean. In subsection 3.4, we check the flux calibration by comparing the line ratios of the SDSS and LRS2 spectra and find offsets ranging from  $0\sigma$  to  $3\sigma$  between the two datasets.

### 3 EMISSION LINE PARAMETER ESTIMATION

Here we describe the techniques used to derive emission line properties from the observations described in subsection 2.1. We first defined apertures for the spectral extraction (subsection 3.1), removed the continuum from the spectra (subsection 3.2), fit the emission lines (subsection 3.3), and corrected for dust attenuation (subsection 3.5). Our analysis was primarily done using the SPECUTILS, SPECTRALCUBE (Astropy Collaboration et al. 2018), and LMFIT (Newville et al. 2014) python packages.

#### 3.1 Apertures

A primary goal of this work is to test the impact of geometry and spatial distribution on the resonant Mg II emission. To do this, we extract the spectral information from spatially distinct apertures within the LRS2 data cube that are separated by more than the convolved seeing of the observations. Doing this leaves us with 5 spaxel radius (1.25 arcsec, 12.5 kpc diameter) apertures, as dictated by the seeing of the observations in subsection 2.1. Given this aperture size, we optimized the number of apertures while maximizing the delivered signal-to-noise by extracting our signal from four spatially distinct regions. These regions covered the extent of J0919 without sampling the center multiple times, as seen in Figure 1.

While the center-most aperture (radius of 1 arcsec) does overlap with the other apertures, it allows for the LRS2 data to be compared to other data sets in the literature. The large aperture, referred to as the "Integrated aperture", maximizes the SNR of our observations. We extracted the spectra by summing the flux in each aperture. Figure 2 shows the lines we extracted from our spatially distinct apertures.

#### 3.2 Continuum fit

To ensure the measured emission line properties did not contain contributions from the stellar and nebular continua, we first had to remove the continuum. For our continuum fitting procedure, we used the FIT\_CONTINUUM function from the SPECUTILS package. We modified the default Chebyshev model to be 1st order instead of 3rd order to better match the observed continuum shape. In order to fit the continuum, we visually picked a region on either side of the emission line that was in close proximity to the line but did not contain any absorption/emission features. This procedure was applied to the spectra extracted in the different apertures. The residual emission flux was then obtained by subtracting the resulting continuum models.

Stellar population models suggest that young stellar populations have a  $\sim 2\text{ \AA}$   $H\beta$  equivalent width (González Delgado et al. 1999). J0919 has a measured  $H\beta$  equivalent width of  $435\text{ \AA}$  (Izotov et al. 2021). This extreme value indicates that the stellar population is

very young. The change in  $H\beta$  equivalent width caused by stellar population models would be of less than 0.5% for J0919. Further, with the continuum not being significantly detected underneath the Balmer lines (see Figure 3 bottom row, third panel), we conclude that there is little contribution from stellar absorption.

#### 3.3 Emission line fit

Our method to measure the emission line parameters consisted of using LMFIT and a bootstrap Monte Carlo method. More precisely, we use the MINIMIZE() function and a Gaussian model with parameters of line center, line width, and amplitude to achieve all of our fits. The lower limit for the line width of our fits was based on the spectral resolution of each LRS2 arm (see subsection 2.1 for the limits). This work focuses on the integrated fluxes. Subsequent work will study the kinematic information of the emission lines.

For our bootstrap Monte Carlo method, we first estimated the noise level by calculating the standard deviation of the continuum-subtracted data (see subsection 3.2) in two 80-100 pixel-wide spectral windows directly adjacent to each individual emission line. With the NUMPY.RANDOM.NORMAL() function (Harris et al. 2020), we generated 1000 realizations of the extracted spectrum where each flux density is randomly drawn from a normal distribution centered on the original flux density value with a standard deviation given by the estimated noise value calculated above. We then fit a Gaussian to each of the 1000 modified spectra. Our initial values came from the SPECUTILS FIND\_LINES\_THRESHOLD function.

We tabulated the results and took the mean and standard deviation of the distribution. The results of these calculation are reported in Table 1. These techniques allowed us to measure the properties and errors of the emission lines of interest in a consistent way. Examples of our fits can be found in Figure 3. Table 1 gives the observed and extinction corrected fluxes (subsection 3.5), respectively, for 9 different measured emission lines in our 6 different apertures.

All conversions from wavelengths to velocities were done using the restframe wavelengths from the NIST Atomic Spectra Database Lines Form (Kramida et al. 2021). The lines measured in this work were Mg II, [O II] $\lambda 3728$ , [Ne III] $\lambda 3869$ , H $\gamma$ , [O III] $\lambda 4363$ ,  $H\beta$ , [O III] $\lambda 4959$ , [O III] $\lambda 5007$ , and  $H\alpha$ .

#### 3.4 Comparison of fluxes and ratios to previous work

To compare the LRS2 observations presented here to other literature measurements, we extracted the LRS2 flux from a  $2''$  aperture, centered on the peak emission within J0919 (called the central aperture; the center most aperture in Figure 1). This aperture matches the  $2''$  diameter of the BOSS fibers (Smee et al. 2013). We then downloaded the calibrated spectra from the Sloan Digital Sky Survey DR15 (Aguado et al. 2019) and measured the emission line properties in the same way as was done in Sections 3.2-3.5 with the LRS2 data. Our values from the SDSS spectra match literature values for integrated flux, equivalent width, and E(B-V) within  $1.5\sigma$  for all emission lines (Flurry et al. submitted, Izotov et al. 2021).

Table 3 compares the emission line ratios measured from the LRS2 (top row) and SDSS (bottom row) spectra. Most of the values measured from LRS2 match what we measured from the SDSS. There are two exceptions. We measured a value of  $3.95 \pm 0.02$  for the  $H\alpha/H\beta$  from the LRS2 data. This is inconsistent with the value we measured from the SDSS data of  $2.97 \pm 0.03$ . Our value for the [O III] $\lambda 5007$ /[O II] $\lambda 3728$  ratio is also inconsistent with the SDSS measurement. Both the  $H\alpha$  and [O III] $\lambda 5007$  lines are observed in the Red arm, while the other

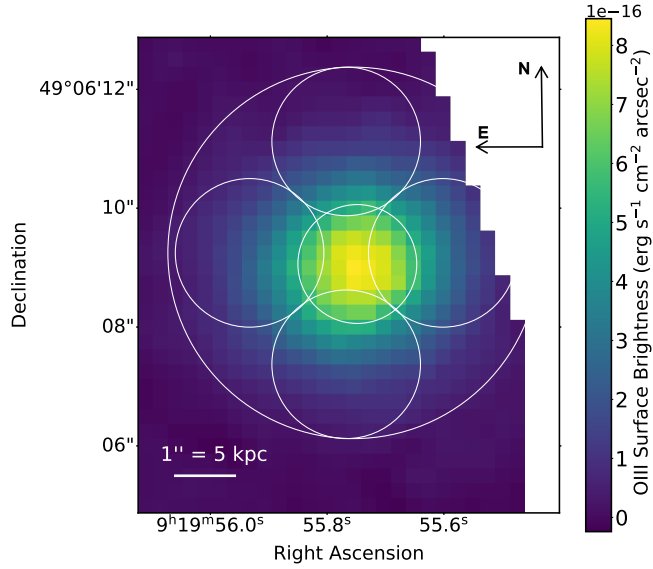


**Figure 1.** The continuum subtracted surface brightness spatial map for [O III]λ5007. The largest aperture is referred to as the Integrated aperture and the others are named after their position relative to the galaxy center (e.g. the aperture at the top of the image is the Top aperture). We include a 1'' scale bar, where 1'' corresponds to approximately 5 kpc in the frame of the galaxy.

lines discussed here are on the Blue arm of LRS2. This suggests a slight flux calibration offset between the Blue and Red arms of LRS2. There may be a slight absolute flux calibration between the Red and the Blue arms making lines in the red arm appear brighter than the blue arm, however, the relative flux calibration appears to be robust and consistent across the apertures. This means that the offset in the flux ratios will be similarly offset within the LRS2 observations, but may not be directly comparable to emission line measurements from other instruments.

To estimate the dust attenuation, it is crucial to have flux estimates on consistent flux scales. The H $\beta$  and H $\gamma$  lines are both observed in LRS2-Blue and both the SDSS and LRS2 obs. agree (see Table 2). This consistency indicates that the H $\gamma$  and H $\beta$  ratio can be used to infer the dust attenuation. This is why we used the  $\frac{H\gamma}{H\beta}$  ratio instead of  $\frac{H\alpha}{H\beta}$  to determine the dust attenuation. We used a redshift value of 0.40512 from SDSS in our calculations but most of the LRS2 emission lines are slightly offset from this systemic value (by  $\sim 10 \text{ km s}^{-1}$ ). With our measurements matching other independent measurements, we can move forward assuming accurate results from our analysis.

### 3.5 Dust extinction correction

We corrected the continuum subtracted emission-line flux values to account for the impact of dust present in the Milky Way (MW) and J0919. Dust extinction reduces the amount of flux that reaches our telescope by absorbing and/or scattering the photons of interest. It is also wavelength dependent meaning very blue lines, like Mg II, are more reduced than redder lines like H $\beta$ . Correcting for dust extinction and comparing to uncorrected values constrains the spatial distribution of dust and reveals the intrinsic nebular conditions (e.g. metallicity, ionization structure, etc.). The correction was done using the following steps:

- (i) Corrected the flux based on J0919's position in the Milky Way

(MW) by multiplying the flux by:

$$10^{0.4 \times E(B-V)_{\text{MW}} \times k(\lambda_{\text{obs}})}, \quad (2)$$

where  $E(B-V)_{\text{MW}}$  is the MW color excess, which has a value of 0.029 (Green et al. 2019), and  $k(\lambda_{\text{obs}})$  is the value of the CCM89 extinction law at the observed wavelength of each individual emission line (Cardelli et al. 1989).

- (ii) Calculated the color excess from J0919 using equation A8 from (Rosa-González et al. 2002)

$$E(B-V) = \frac{\log 0.47 - \log \frac{F(H\gamma)}{F(H\beta)}}{0.4[k(F(H\gamma)) - k(F(H\beta))]} \quad (3)$$

We determine  $E(B-V)$  using  $F(H\gamma)$  and  $F(H\beta)$ , which are the continuum subtracted and MW dust attenuation corrected H $\gamma$  and H $\beta$  fluxes from each aperture. The value of 0.47 is the intrinsic  $\frac{H\gamma}{H\beta}$  ratio with no dust attenuation (Osterbrock 1989). This value assumes a temperature of  $10^4 \text{ K}$  and a density of  $100 \text{ cm}^{-3}$ . The values of  $k(H\gamma)$  and  $k(H\beta)$  are the values of the CCM89 extinction law at the rest wavelength values of H $\gamma$  and H $\beta$  (4340Å and 4861Å respectively). See Table 1 for the  $E(B-V)$  values for each aperture. To avoid non-physical values, we capped the values of  $E(B-V)$  to 0. This cap only affected the top aperture.

- (iii) To correct for dust in J0919 we multiplied the MW corrected fluxes by:

$$10^{0.4 \times E(B-V) \times k(\lambda_{\text{rest}})} \quad (4)$$

where  $k(\lambda_{\text{rest}})$  is the value of the CCM89 extinction law at the rest wavelength of each individual emission line. We did not correct the values in the [O III]λ5007 spatial map (see Figure 1) in order to retain the observed spatial extent of J0919. However, we did apply these corrections to all the rows marked with "Cor" in Table 1. This was done to highlight spatial differences between the apertures.

### 3.6 Determining metallicities

For each aperture we used PYNEB (Luridiana et al. 2014) and the extinction-corrected [O III]λ5007, [O III]λ4363, [O II]λ3727 fluxes, all normalized by the H $\beta$  flux, to calculate the Oxygen abundances using the direct- $T_e$  method (Garnett (1992), Berg (2013)). To determine the electron temperature, we used the temperature sensitive ratio of [O III]λ5007 to the auroral [O III]λ4363 line. Our calculated electron temperatures range from 14000-15804 K. We then used the [O II]λ3727 and [O III]λ5007 fluxes, relative to H $\beta$ , to determine the oxygen abundances in the intermediate (for [O II]λ3727) and high-ionization (for [O III]λ5007) zone by assuming a single temperature across the H II region. By considering the total oxygen abundance as the sum of the intermediate and high ionization zones, we calculated the total oxygen abundance. This is a good approximation for galaxies that are as highly ionized as our target.

We detect the [O III]λ4363 line at  $> 4\sigma$  significance in all of our apertures and list the inferred metallicity in each aperture in the last column of Table 2 as  $12 + \log(\text{O/H})$ . Izotov et al. (2021) calculated an electron temperature of  $16660 \pm 1440$  and a metallicity of  $7.77 \pm 0.01$ . These values are  $3\sigma$  from our measurements in the central aperture (Table 2).

## 4 RESULTS

In this section we use the H $\gamma$  and H $\beta$  fluxes along with the attenuation-corrected flux [O III]λ5007 and [O II]λ3728 to measure



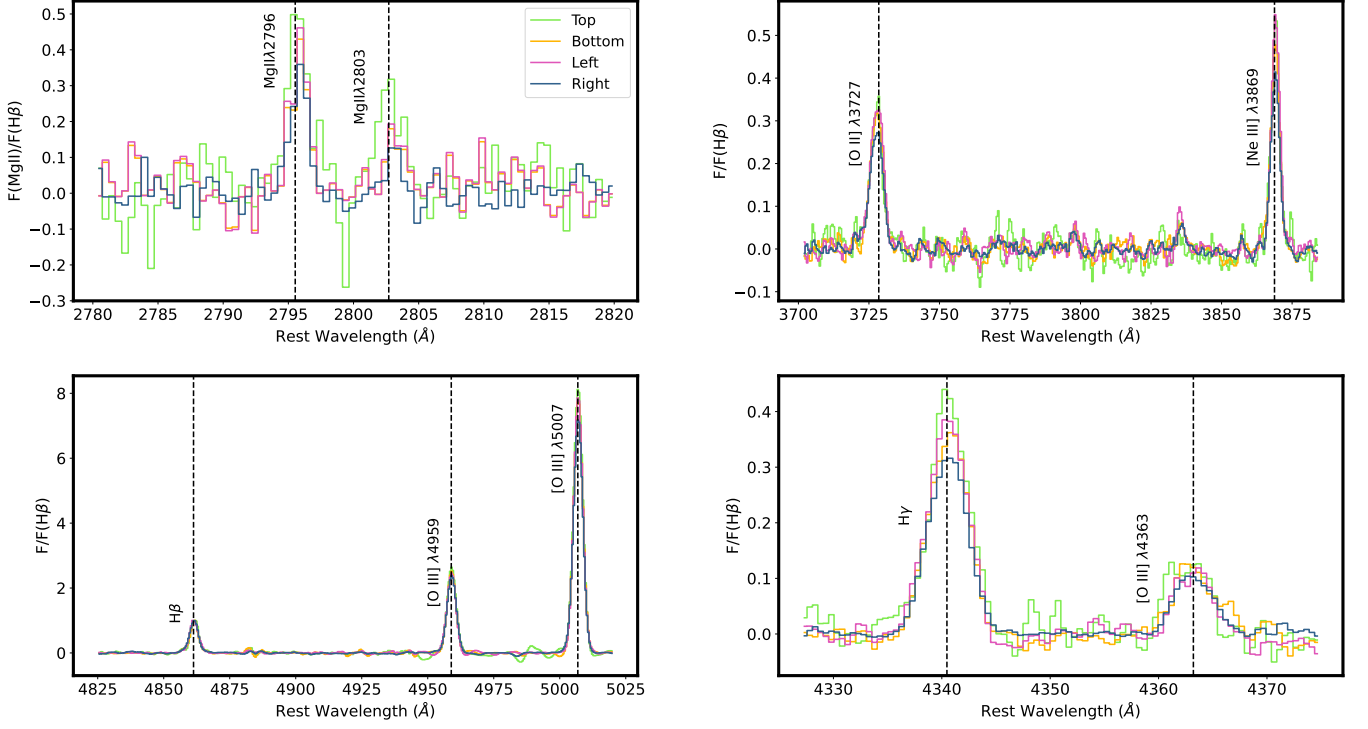


**Figure 2.** The restframe spectra of Mg II, [O III]  $\lambda 3728$ , [Ne III]  $\lambda 3869$ , H $\gamma$ , [O III]  $\lambda 4363$ , H $\beta$ , [O III]  $\lambda 4959$ , and [O III]  $\lambda 5007$  from each aperture, overlaid on one another. The flux densities were continuum subtracted but not dust extinction corrected. The flux densities were normalized by the maximum H $\beta$  flux density in their respective aperture such that all flux densities are relative to H $\beta$ . The vertical dashed lines represent the rest wavelength line center.

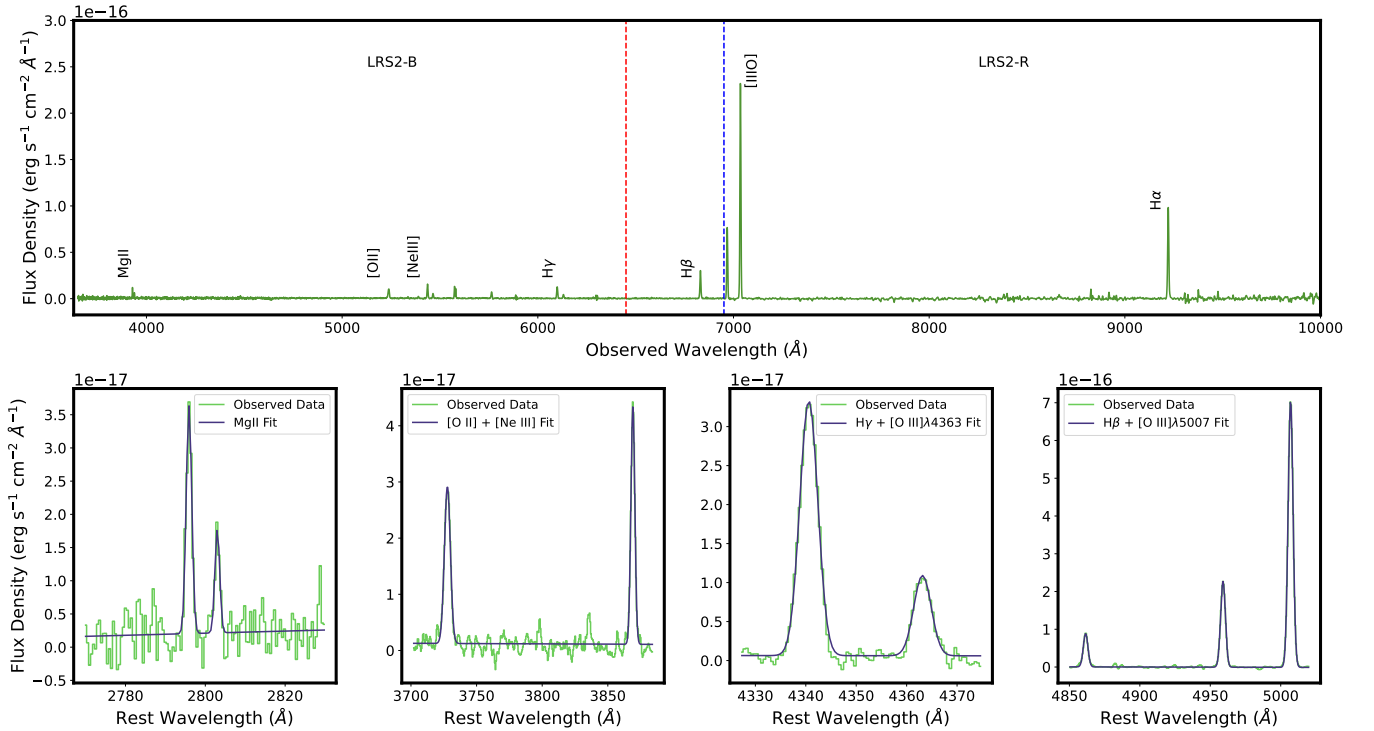


**Figure 3.** *Top:* the complete observed spectra from the Integrated aperture with a few lines of interest labelled. The blue dashed line marks the end of LRS2-B and the red dashed line marks the beginning of LRS2-R. *Bottom:* A zoom in on some emission line fits with the restframe observed spectra in green and the fit in purple. The lines that we fit are: Mg II, [O II]  $\lambda 3728$ , [Ne III]  $\lambda 3869$ , H $\gamma$ , [O III]  $\lambda 4363$ , H $\beta$ , [O III]  $\lambda 4959$ , [O III]  $\lambda 5007$ , and H $\alpha$ .

dust extinction and ionization. In the following subsections we compare ionization ( $[\text{O III}]\lambda 5007/[\text{O II}]\lambda 3728$ ) to dust ( $H\gamma/H\beta$ ), dust to  $\text{Mg II}\lambda 2796$ , and ionization to  $\text{Mg II}\lambda 2796$ . While our 6 apertures represent too small of a sample to be statistical, this analysis aims to quantify the spatial variation of  $\text{Mg II}$  within a single LyC emitting galaxy, at  $z \approx 0.4$ , to assess the spatial variation of the LyC escape.

#### 4.1 Integrated and resolved galaxy properties

Our observations of J0919 as a whole are contained in the Integrated aperture. From Table 1, the integrated  $\text{Mg II}$  flux is  $1.68 \times 10^{-16} \text{ erg s}^{-1} \text{ cm}^{-2}$  and the integrated  $\text{Mg II}$  luminosity is  $1.01 \times 10^{41} \text{ erg s}^{-1}$ . These values are larger than those measured in the Central aperture and by extension, indicate that the SDSS data may not measure all of the  $\text{Mg II}$  flux. The other values of interest from the Integrated aperture, found in Table 2, are:  $[\text{O III}]\lambda 5007/[\text{O II}]\lambda 3728 = 13.6 \pm 0.4$ ;  $H\gamma/H\beta = 0.407 \pm 0.008$ ;  $12 + \log(\text{O}/\text{H}) = 8.02 \pm 0.07$ ; and  $E(B-V) = 0.26 \pm 0.04$ . On a smaller scale than the Integrated aperture, Figure 2 overlays the  $H\beta$ -normalized-spectra of the spatially distinct apertures. From this comparison a visual difference can be seen between the different spectra; Differences which indicate that the emission features vary per region. Specifically in the case of  $H\gamma/H\beta$  (which is used to calculate dust attenuation; see subsection 3.5), the spectra span As a comparison of our spatially distinct apertures, Figure 2 demonstrates significant variations in many of the emission lines. These variations are investigated in terms of dust and ionization properties in the next subsections.

#### 4.2 Relationship between ionization and dust

Within the frame of understanding local LyC escape, we explored the relationship between ionization and dust in each aperture. Ionization is important for LyC escape because galaxies that are more ionized have less relative neutral hydrogen. We use the  $[\text{O III}]\lambda 5007/[\text{O II}]\lambda 3728$  ratio because this ratio directly traces the fraction of highly ionized to moderately ionized gas. As such it is a diagnostic of the ionization state of the gas, with higher  $[\text{O III}]\lambda 5007/[\text{O II}]\lambda 3728$  values corresponding to more highly ionized nebulae. Dust preferentially absorbs and scatters bluer wavelengths, meaning that it strongly absorbs ionizing photons. This relationship is shown in Figure 4. Our dust ratios consist of the observed  $H\gamma$  and  $H\beta$  fluxes, where a ratio of 0.47 represents a dust free nebula (Osterbrock 1989). These uncorrected fluxes give us a direct measurement of the impact of dust. The  $[\text{O III}]\lambda 5007$  and  $[\text{O II}]\lambda 3728$  fluxes were corrected for dust attenuation because we were interested in the intrinsic ionization of the aperture. We measure different ionization and dust attenuation values for each aperture and find spatial variations between the apertures. We also find a negative trend between ionization and dust (note that dust content increases towards lower  $H\gamma/H\beta$  values while ionization decreases towards lower values). This trend indicates that regions within J0919 with less dust are more highly ionized. We discuss the implications for this trend in subsection 5.1. The central and integrated apertures are included in our measurements because of the extra information they provide. The central aperture is where the HST/COS observations of the LyC are for J0919.

#### 4.3 Relationship between dust and $\text{Mg II}\lambda 2796$ flux

There are two sinks for ionizing photons: dust and gas. One of our goals is to explore the relative impact of both dust and neutral gas on a

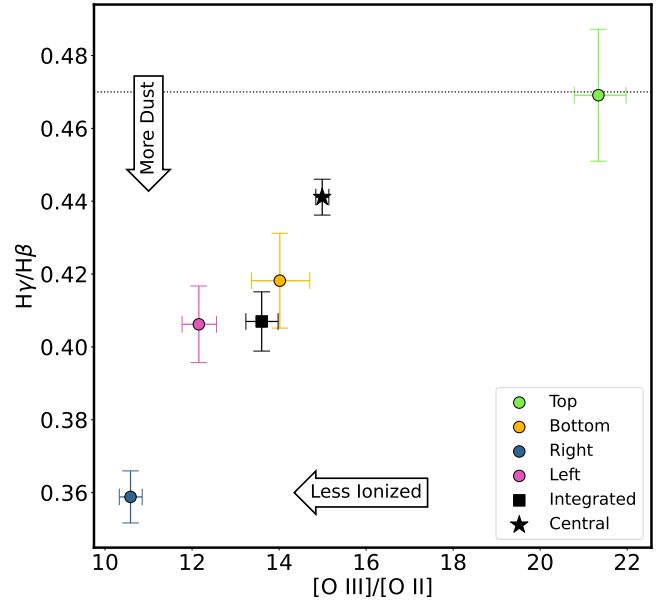


**Figure 4.** The  $H\gamma/H\beta$  ratio of the individual apertures versus the  $[\text{O III}]\lambda 5007/[\text{O II}]\lambda 3728$  ratio. The  $H\gamma/H\beta$  ratio traces dust attenuation and the  $[\text{O III}]\lambda 5007/[\text{O II}]\lambda 3728$  ratio traces ionization. Dust content increases with deviations from 0.47 (see arrows). The dotted line is at a value of 0.47 and corresponds to a dust free region. The legend caption refers to the aperture location.

spatial basis within J0919. We can explore neutral gas using the  $\text{Mg II}$  doublet ratio or photoionization models (Henry et al. 2018; Chisholm et al. 2020). The two  $\text{Mg II}$  transitions ( $\text{Mg II}\lambda 2796$  and  $\text{Mg II}\lambda 2803$ ) have different oscillator strengths. This means that their observed relative flux ratios are sensitive to the  $\text{Mg II}$  column density. However, the SNR of  $\text{Mg II}\lambda 2803$  averages 3, which is too low to allow for an analysis using the doublet ratio technique on a spatially resolved basis (see Table 1). Because we do not use  $\text{Mg II}\lambda 2803$ , any mention of  $\text{Mg II}$  in the rest of the paper will be referring to  $\text{Mg II}\lambda 2796$  exclusively. We note, however, that the total integrated flux ratio that we measured ( $2.6 \pm 0.6$ , see Table 1) suggests that  $\text{Mg II}$  photons are on average escaping in an optically thin medium (Chisholm et al. 2020). In place of the doublet ratio we take the observed  $\text{Mg II}\lambda 2796$  values and normalize them by the dust attenuation corrected  $[\text{O III}]\lambda 5007$  values. The fraction of  $\text{Mg II}\lambda 2796$  emission we observe relative to the  $[\text{O III}]$  emission is related to the neutral gas column density (Henry et al. 2018). This enables us to study the relationship between neutral gas column density and the dust attenuation as well as compare our values to photoionization models. The relationship between neutral gas column density and ionization is presented in the next subsection.

We measure significant  $\text{Mg II}\lambda 2796$  flux variation for each aperture (Figure 5). The  $\text{Mg II}\lambda 2796$  line, normalized by the  $[\text{O III}]\lambda 5007$  line, is positively correlated with the  $H\gamma/H\beta$  ratio. More  $\text{Mg II}\lambda 2796$  relative to  $[\text{O III}]$  emission escapes the galaxy in less dusty regions of J0919. In Section 5.1 we use photoionization models to explore how this observation relates to the escape of ionizing photons.

#### 4.4 Relationship between ionization and $\text{Mg II}\lambda 2796$ flux

The ionization state of the gas traces the amount of low ionization relative to high ionization gas. In regions with high ionization there is less neutral gas that can absorb LyC photons and the

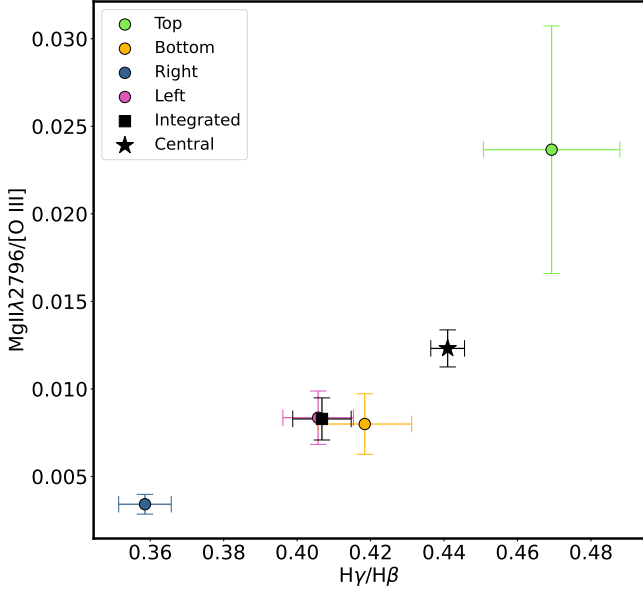


**Figure 5.** The  $\frac{H\gamma}{H\beta}$  flux ratio of the different apertures versus the  $Mg\ II\ \lambda 2796$  flux, normalized by the  $[O\ III]\ \lambda 5007$  flux. The  $\frac{H\gamma}{H\beta}$  flux ratio traces dust attenuation and has an intrinsic value of 0.47 in the absence of dust. Regions within J0919 with the highest observed  $Mg\ II/[O\ III]\ \lambda 5007$  ratios also have the lowest dust attenuation. The legend caption refers to the aperture location within J0919.

$Mg\ II\ \lambda 2796/[O\ III]\ \lambda 5007$  ratio allows for a comparison between the observed  $Mg\ II$  values and the predicted values from the photoionization models of Henry et al. (2018) (see subsection 5.1).

In each of our apertures, we measure different ionization and  $Mg\ II\ \lambda 2796$  flux values. Figure 6 shows a positive trend between ionization, measured with the dust attenuation corrected  $[O\ III]\ \lambda 5007/[O\ II]\ \lambda 3728$  ratio, and the observed  $Mg\ II\ \lambda 2796$  flux, which was normalized by the dust attenuation corrected  $[O\ III]\ \lambda 5007$  flux. This indicates that regions within J0919 that have the highest  $Mg\ II$  relative to  $[O\ III]$  emission are also the most ionized. We find similar trends with the  $[Ne\ III]\ \lambda 3869/[O\ II]\ \lambda 3728$  flux ratios (see Table 2) but use the  $[O\ III]\ \lambda 5007/[O\ II]\ \lambda 3728$  ratio because  $[O\ III]\ \lambda 5007$  has significantly higher SNR than  $[Ne\ III]\ \lambda 3869$ .

From Figure 6, we see that the central aperture is more transparent in its emission of  $Mg\ II\ \lambda 2796$  flux than the average for J0919, but it is not as transparent as the top aperture. The integrated aperture represents the “total”  $Mg\ II$  escape of J0919. The  $Mg\ II\ \lambda 2796$  escape fraction of the integrated aperture is nearly the average of all the other apertures (Table 4; subsection 5.3).

## 5 DISCUSSION

In this section we comment on the variations in our different apertures using the quantities in Tables 1 and 2. We also discuss the implications of the trends between dust, ionization, and  $Mg\ II$  from section 4 on the escape of  $Mg\ II$  and LyC photons.

### 5.1 Ionization, dust, and escape fractions

To better understand how  $Mg\ II$  serves as a means to trace neutral H and the escape of ionizing photons, we study the spatial variation of  $Mg\ II$ . Confirming methods to infer the LyC escape fraction

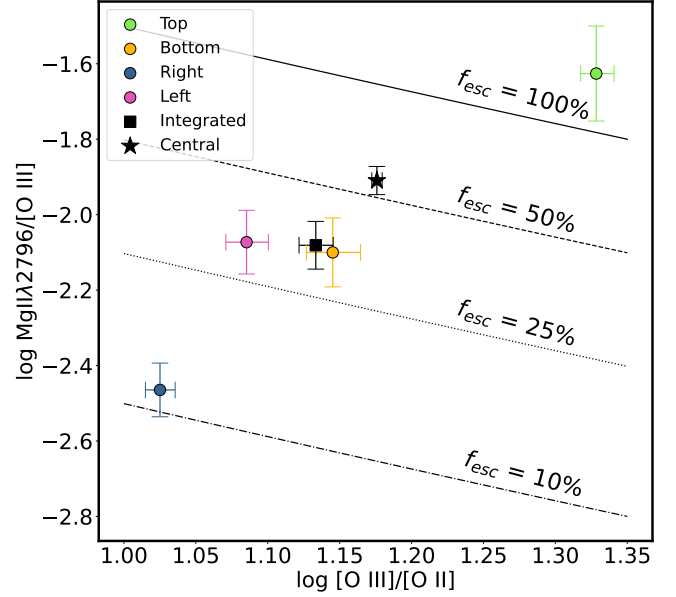


**Figure 6.** The ionization of the galaxy measured with the  $[O\ III]\ \lambda 5007/[O\ II]\ \lambda 3728$  ratio versus the  $Mg\ II\ \lambda 2796$  flux, normalized by the  $[O\ III]\ \lambda 5007$  flux. The lines represent different  $Mg\ II\ \lambda 2796$  escape fractions (Henry et al. 2018). Regions within J0919 with the highest ionization have the largest  $Mg\ II$  escape fractions. The legend caption refers to the aperture location.

locally, would allow us to determine how the distant universe was reionized. In Section 4, we show that there are significant relations between the  $Mg\ II$  emission and both the nebular ionization and the dust attenuation. These correlations suggest that a larger fraction of  $Mg\ II$  escapes regions of higher ionization and lower dust attenuation (Figure 5, Figure 6). Both of these conditions are consistent with  $Mg\ II$  being a strong tracer of LyC escape because both dust and low-ionization (neutral) gas absorbs ionizing photons (Chisholm et al. 2020). While these empirical trends suggest that more  $Mg\ II$  photons, and by extension LyC photons, will escape highly ionized, dust-free regions, it does not tell us what fraction of  $Mg\ II$  escapes these regions.

To calculate the  $Mg\ II$  escape fractions, we used equation 1 from Henry et al. (2018) and our dust attenuation corrected  $[O\ III]\ \lambda 5007/[O\ II]\ \lambda 3728$  ratio to calculate the intrinsic  $Mg\ II\ \lambda 2796/[O\ III]\ \lambda 5007$  ratio. We calculated our observed  $Mg\ II\ \lambda 2796/[O\ III]\ \lambda 5007$  ratio with the observed  $Mg\ II\ \lambda 2796$  flux and the dust attenuation corrected  $[O\ III]\ \lambda 5007$  flux. The ratio of our observed  $Mg\ II/[O\ III]$  ratio to the intrinsic ratio is our reported  $Mg\ II$  escape fraction (see Table 4). Combining Figure 5 and Figure 6, we find that regions within J0919 with low dust attenuation that are highly ionized emit roughly 100% of their intrinsic  $Mg\ II$  emission, while regions that are lower ionization and higher dust attenuation emit  $\sim 10\%$  of their intrinsic  $Mg\ II$  emission. This factor of  $\sim 10$  difference in  $Mg\ II$  escape fraction illustrates that there are strong spatial variations in the  $Mg\ II$  escape (we discuss this more in the next section).

Finally, we follow Chisholm et al. (2020) to extend the  $Mg\ II$  escape fraction to the LyC escape fraction by dust correcting the  $Mg\ II$  escape fraction (Table 4). To do this, we convert the  $E(B-V)$  that was inferred using the Cardelli et al. (1989) attenuation curve to one using the Reddy et al. (2016) reddening curve and then use the value of the Reddy et al. (2016) attenuation law at 912 ( $k(912) =$

**Table 1.** E(B-V) values, attenuation corrected integrated fluxes, and observed integrated fluxes for 6 different apertures and 9 different emission lines. The fluxes are in units of ( $10^{-16}$  erg s $^{-1}$  cm $^{-2}$ ). E(B-V) is in units of magnitudes. Cor indicates that the values have been attenuation corrected. The aperture naming convention refers to the aperture's position relative to the galaxy's center (see legend of Figure 2) where the integrated aperture is the largest aperture in Figure 1.

Region	E(B-V)	Mg II $\lambda$ 2796	Mg II $\lambda$ 2803	[O II] $\lambda$ 3728	[Ne III] $\lambda$ 3869	H $\gamma$	[O III] $\lambda$ 4363	H $\beta$	[O III] $\lambda$ 5007
Integrated	-	1.2 $\pm$ 0.1	0.48 $\pm$ 0.01	3.23 $\pm$ 0.05	3.35 $\pm$ 0.04	2.95 $\pm$ 0.05	0.9 $\pm$ 0.5	7.26 $\pm$ 0.08	61.40 $\pm$ 0.09
Integrated <sup>Cor</sup>	0.26 $\pm$ 0.04	6 $\pm$ 1	2.3 $\pm$ 0.7	11 $\pm$ 2	11 $\pm$ 2	8.6 $\pm$ 1.3	2.6 $\pm$ 0.4	18 $\pm$ 2	150 $\pm$ 18
Top	-	0.19 $\pm$ 0.03	0.14 $\pm$ 0.04	0.34 $\pm$ 0.02	0.43 $\pm$ 0.01	0.38 $\pm$ 0.01	0.12 $\pm$ 0.01	0.81 $\pm$ 0.02	7.38 $\pm$ 0.04
Top <sup>Cor</sup>	0.00 $\pm$ 0.07	0.2 $\pm$ 0.1	0.16 $\pm$ 0.08	0.4 $\pm$ 0.1	0.5 $\pm$ 0.2	0.4 $\pm$ 0.1	0.13 $\pm$ 0.04	0.9 $\pm$ 0.2	7.8 $\pm$ 1.9
Bottom	-	0.21 $\pm$ 0.02	0.10 $\pm$ 0.07	0.70 $\pm$ 0.02	0.73 $\pm$ 0.02	0.62 $\pm$ 0.02	0.24 $\pm$ 0.02	1.48 $\pm$ 0.03	12.91 $\pm$ 0.03
Bottom <sup>Cor</sup>	0.21 $\pm$ 0.06	0.8 $\pm$ 0.3	0.4 $\pm$ 0.3	1.9 $\pm$ 0.5	1.9 $\pm$ 0.5	1.5 $\pm$ 0.3	0.6 $\pm$ 0.1	3.1 $\pm$ 0.6	26 $\pm$ 5
Right	-	0.29 $\pm$ 0.03	0.11 $\pm$ 0.05	0.81 $\pm$ 0.02	0.82 $\pm$ 0.01	0.74 $\pm$ 0.01	0.23 $\pm$ 0.01	2.06 $\pm$ 0.03	15.95 $\pm$ 0.03
Right <sup>Cor</sup>	0.50 $\pm$ 0.04	5 $\pm$ 1	2 $\pm$ 1	8 $\pm$ 1	8 $\pm$ 1	5.5 $\pm$ 0.8	1.7 $\pm$ 0.3	12 $\pm$ 2	85 $\pm$ 10
Left	-	0.24 $\pm$ 0.03	0.11 $\pm$ 0.06	0.70 $\pm$ 0.02	0.72 $\pm$ 0.01	0.61 $\pm$ 0.01	0.17 $\pm$ 0.01	1.51 $\pm$ 0.01	11.96 $\pm$ 0.03
Left <sup>Cor</sup>	0.26 $\pm$ 0.05	1.2 $\pm$ 0.3	0.5 $\pm$ 0.3	2.4 $\pm$ 0.5	2.5 $\pm$ 0.5	1.8 $\pm$ 0.3	0.5 $\pm$ 0.1	3.9 $\pm$ 0.6	30 $\pm$ 4
Central	-	0.40 $\pm$ 0.02	0.14 $\pm$ 0.02	1.25 $\pm$ 0.02	1.29 $\pm$ 0.01	1.22 $\pm$ 0.01	0.41 $\pm$ 0.01	2.76 $\pm$ 0.01	21.87 $\pm$ 0.03
Central <sup>Cor</sup>	0.10 $\pm$ 0.02	0.8 $\pm$ 0.1	0.27 $\pm$ 0.05	2.2 $\pm$ 0.2	2.2 $\pm$ 0.2	2.0 $\pm$ 0.2	0.66 $\pm$ 0.05	4.2 $\pm$ 0.3	33 $\pm$ 2

**Table 2.** Emission line flux ratios for the 6 different apertures. All fluxes are dust extinction corrected except for the Mg II, H $\alpha$ /H $\beta$ , and H $\gamma$ /H $\beta$  ratios.

Region	Mg II $\lambda$ 2796/Mg II $\lambda$ 2803	[O III] $\lambda$ 5007/[O II] $\lambda$ 3728	Mg II $\lambda$ 2796/[O III] $\lambda$ 5007	[Ne III] $\lambda$ 3869/[O II] $\lambda$ 3728	H $\gamma$ /H $\beta$	12+log(O/H)
Integrated	2.6 $\pm$ 0.6	13.6 $\pm$ 0.4	0.008 $\pm$ 0.001	1.006 $\pm$ 0.03	0.407 $\pm$ 0.008	8.02 $\pm$ 0.07
Top	1.3 $\pm$ 0.4	21.3 $^{+0.6}_{-0.7}$	0.024 $\pm$ 0.007	1.3 $^{+0.1}_{-0.9}$	0.47 $\pm$ 0.02	8.1 $\pm$ 0.1
Bottom	2 $\pm$ 1	14.0 $^{+0.6}_{-0.7}$	0.008 $\pm$ 0.002	1.01 $\pm$ 0.04	0.42 $\pm$ 0.01	7.9 $\pm$ 0.1
Right	2.7 $\pm$ 1.4	10.6 $\pm$ 0.3	0.0034 $\pm$ 0.0006	0.97 $\pm$ 0.03	0.359 $\pm$ 0.007	7.90 $\pm$ 0.07
Left	2.3 $\pm$ 1.4	12.1 $^{+0.3}_{-0.4}$	0.008 $\pm$ 0.002	1.002 $^{+0.04}_{-0.03}$	0.41 $\pm$ 0.01	8.0 $\pm$ 0.1
Central	3.0 $\pm$ 0.5	15.0 $\pm$ 0.1	0.012 $\pm$ 0.001	1.01 $\pm$ 0.02	0.441 $\pm$ 0.005	7.92 $\pm$ 0.04

**Table 3.** Values from our measurements in the LRS2 2'' aperture and the SDSS spectra. The 2'' aperture is the central aperture in Figure 1. No fluxes have been dust corrected and the E(B-V) values were calculated using Equation 3.

Instrument	H $\gamma$ /H $\beta$	H $\gamma$ /H $\beta$ E(B-V)	Mg II 2796/Mg II 2803	H $\alpha$ /H $\beta$	[O III] $\lambda$ 5007/[O II] $\lambda$ 3728	[O III] $\lambda$ 5007/[O III] $\lambda$ 4959
LRS2 2''	0.441 $\pm$ 0.005	0.11 $\pm$ 0.02	3.0 $\pm$ 0.5	3.95 $\pm$ 0.02	17.4 $\pm$ 0.2	3.11 $\pm$ 0.01
SDSS	0.44 $\pm$ 0.01	0.10 $\pm$ 0.06	1.9 $\pm$ 0.5	2.97 $\pm$ 0.03	12.3 $\pm$ 0.3	3.05 $\pm$ 0.02

**Table 4.** Values from our measurements of the Mg II and LyC escape fractions along with the ionizing photon escape estimate,  $F_{\text{esc,LyC}} * F(\text{H}\beta)$ , for the 6 individual apertures and the average of the spatially distinct regions. All the escape fractions are percentages.  $F(\text{H}\beta)$  is the extinction corrected H $\beta$  flux.  $F_{\text{esc,LyC}} * F(\text{H}\beta)$  has units of ( $10^{-18}$  erg s $^{-1}$  cm $^{-2}$ ), except for the Average value. The average is weighted by  $F(\text{H}\beta)$ , making it unitless.

Region	Mg II Escape	LyC Escape	$F_{\text{esc,LyC}} * F(\text{H}\beta)$
Integrated	34 $\pm$ 6	0.2 $\pm$ 0.2	4 $\pm$ 3
Top	100 $\pm$ 50	100 $\pm$ 210	90 $\pm$ 180
Bottom	34 $\pm$ 8	0.6 $\pm$ 0.7	2 $\pm$ 2
Right	11 $\pm$ 2	0.0008 $\pm$ 0.0006	0.009 $\pm$ 0.007
Left	32 $\pm$ 7	0.2 $\pm$ 0.2	0.8 $\pm$ 0.8
Central	56 $\pm$ 5	8 $\pm$ 3	32 $\pm$ 13
Average	44 $\pm$ 3	0.3 $\pm$ 0.5	0.05 $\pm$ 0.09

12.87). Since regions with high dust attenuation already have lower Mg II escape fractions, these regions have five orders of magnitude lower LyC escape fractions than regions with higher Mg II escape. The high dust attenuation and low ionization (more neutral gas) of these regions compound to reduce the LyC escape fractions. Some sightlines through the same galaxy are either transparent or opaque to ionizing photons.

In summary, we find that regions within J0919 that are highly ionized and have low dust attenuation emit a larger fraction of their

intrinsic Mg II, and by extension LyC, photons. The strong correlations found in Figures 4, 5, and 6 illustrate the conditions that are likely to lead to LyC escape are intimately intertwined: low-dust and highly ionized regions within galaxies will have the greatest amounts of Mg II emission.

## 5.2 Variations of indirect tracers between apertures

Recent observations have successfully found local galaxies that emit ionizing photons. These observations have found escape fractions between 0-73%, with a large scatter in many of the classically expected diagnostics – like [O III]  $\lambda$ 5007/[O II]  $\lambda$ 3728 and H $\beta$  equivalent widths (Naidu et al. 2018; Fletcher et al. 2019; Izotov et al. 2021). To reconcile these discrepancies with a complete understanding of Reionization would require a measurement of the volume-averaged escape fraction from LyC leakers. However, all of the direct LyC detections are along a single sightline and do not represent a volume-averaged LyC escape fraction. Three important questions arise from this fact: (a) How can we interpret single sightline LyC escape observations? (b) How representative of a volume-averaged escape fraction is a single LyC detection? (c) Can spatial variations in the LyC escape lead to the scatter observed in the indirect estimators of LyC escape?

In Figure 6, we observe significant spatial variations in the Mg II escape fractions in J0919. Previous work suggests that if we dust



correct the Mg II escape fraction it can predict the LyC escape fractions (see subsection 5.1; Henry et al. (2018); Chisholm et al. (2020)). Since the dust attenuates LyC photons more than Mg II photons and is also correlated with the Mg II/[O III] ratio (Figure 5), this means that the LyC escape fraction varies spatially even more dramatically than the Mg II escape fraction. For example, from the values in Table 4, the top and left apertures differ by a factor of 10 in their Mg II escape fraction. Given that dust preferentially absorbs shorter wavelengths, dust correcting the Mg II escape fractions implies that the LyC escape fractions differ by six orders of magnitude. More concretely, the LyC escape fraction in the right aperture is 0.0008%, while it is approximately 100% in the upper aperture. Izotov et al. (2021) measured a LyC escape fraction of 16% along a single line of sight through the central portion of J0919. This value is consistent with the LyC escape fraction we infer from the central region of J0919 (Table 4). Intriguingly, our Mg II and dust observations imply that if we could measure the LyC escape fraction from a different line of sight within J0919, we would likely infer significantly different LyC escape values. In summary, This suggests that LyC escape fractions are highly sightline dependent and that sightline to sightline variations could introduce significant scatter to both indirect and direct estimates of LyC escape.

Indirect tracers of LyC escape fractions, such as [O III]/[O II], may be less useful due to the scatter introduced by single sightline observations. To quantify this scatter we take the average of the Mg II and LyC escape fractions from all the spatially distinct regions (Top, Bottom, Right, and Left; see Table 4). We estimate that single sightline observations of LyC escape can vary from three to six orders of magnitude around the average value. In stark contrast to this, there is only a factor of 2 difference in the [O III]/[O II] values. This fact implies that at fairly constant [O III]/[O II] values, the line of sight Mg II escape, and by extension LyC escape, can take on vastly different values. Recovering any trends from this amount of scatter would require very large samples.

### 5.3 Single sightlines are unlikely to represent volume averages

Considering the integrated aperture to estimate the LyC escape can reduce the scatter because it would imply a single point can provide an estimate of the observable galaxy (see Table 4). With the Integrated aperture and the midpoint of the scatter within this single galaxy being very similar, one can possibly estimate the integrated escape fraction from the mean of the observations. While the Integrated aperture does not represent the "volume-averaged" escape fraction because we do not see the backside of the galaxy, it does approximate the average escape fraction of the side of the galaxy we see (Table 4).

The central aperture, the brightest and one of the most transparent regions, represents the type of region that is most likely to be probed with single sightline observations. As mentioned above, this region is where the LyC measurement from Izotov et al. (2021) was made. The question is then, how well does our brightest region represent the total escape fraction of the galaxy? The central aperture has  $\sim 1.5$  times higher Mg II escape fraction and  $\sim 40$  times higher LyC escape fraction when compared to both the integrated aperture and the average escape fraction of all the regions. A single sightline observation, especially one of a bright commonly probed region, can result in over, or under, predictions of the average escape fraction of a galaxy (e.g. the Central region and the Right region are dramatically different). Single sightline observations can introduce significant scatter, which makes it crucial to constrain the spatial variation of the escape fraction. For instance, if the Hubble Space Telescope had observed through a different region, it could have estimated an

escape fraction less than 1%, which is no longer above the theorized threshold of 5-20% to be a cosmically relevant source of reionization. Thus, even if a single sightline implies large LyC escape fractions, the entire galaxy may not be emitting sufficient ionizing photons to reionize the Universe.

While a single sightline observation may not produce escape fractions that are representative of the entire galaxy, we can produce estimates of the total amount of reionization-powering photons that escape J0919 to test the single sightline observation. To produce this estimate, we multiply the extinction-corrected H $\beta$  flux ( $F(H\beta)$ ) by the LyC escape fraction for each of the individual regions. This technique can trace reionization because in regions where an electron is ionized off its proton there will be another free proton for the electron to recombine with and emit a recombination line such as H $\beta$ . From only the flux values in Table 1, one might expect that the Central region would dominate in total ionizing photons given that it has four times more  $F(H\beta)$  than the Top region. However, the Top region emits seven times more of its ionizing photons than the Central region. This transparency makes the Top region the largest total emitter of ionizing photons. A caveat to this technique is that in regions that are very optically thin to ionizing photons, like the Top region, the ionizing photons will escape and not ionize the hydrogen, thus reducing the amount of  $F(H\beta)$ . Our estimate of the total ionizing photons from the Top region may be lower than the actual value because of this. Weighting the LyC escape fraction by the H $\beta$  value ensures that the average is pulled towards regions with larger production of ionizing photons. There is a scatter of five orders of magnitude around the average value and no single sightline observation predicts the average across the galaxy.

From our estimates of the escape fractions and the photon counts, we can return, with answers, to the three questions posed above: (a) Single sightline observations do not necessarily provide the escape fraction of an entire galaxy. (b) A single LyC detection does not represent a "volume-averaged" escape fraction and a single sightline can produce escape fractions that are far from a "volume-average". (c) Spatial variation in LyC escape may lead to scatter in indirect estimators of LyC escape. These results rely on one galaxy and similar studies are needed to better investigate the sightline effect.

## 6 SUMMARY AND CONCLUSIONS

In this paper we presented LRS2 spatially resolved spectroscopic observations of Mg II $\lambda$ 2796, Mg II $\lambda$ 2803, [O II] $\lambda$ 3728, [Ne III] $\lambda$ 3869, H $\gamma$ , [O III] $\lambda$ 4363, H $\beta$ , [O III] $\lambda$ 4959, [O III] $\lambda$ 5007, and H $\alpha$  from the previously confirmed  $z \approx 0.4$  LyC emitting galaxy, J0919+4906 (Figure 3). J0919+4906 has an ionizing photon escape fraction of 16% (Izotov et al. 2021).

In order to test the spatial variation of Mg II emission, dust attenuation, and nebular ionization, we separated our data into four spatially distinct apertures and one large aperture to contain all of the signal from our galaxy (subsection 3.1). We include a central aperture to capture the brightest region of the galaxy and to compare our methods to the literature. This central region is where the LyC detection was made in Izotov et al. (2021). The spatially distinct apertures were separated by more than the convolved seeing of the observations (1.25 arcsec; Figure 1). We used the observed Balmer ratios in order to dust attenuation correct our fluxes to have intrinsic values with which to calculate metallicities and escape fractions (Table 2; Table 1).

We observe spatial variations in Mg II emission (taken relative to [O III] $\lambda$ 5007), dust attenuation, and nebular ionization (Figures 2, 4, 5,

and 6). More specifically we find: regions with less dust attenuation are more ionized (Figure 4); regions with more Mg II flux relative to  $[\text{O III}]\lambda 5007$  are more highly ionized and have less dust attenuation (Figures 5 and 6).

From our observed values for ionization and Mg II emission taken relative to  $[\text{O III}]\lambda 5007$ , we use photoionization models to calculate the escape fraction of Mg II (subsection 5.1). We find that there is large spatial variation in the Mg II escape fraction (Table 4). From these variations we find that regions with low dust attenuation and high ionization will have a larger fraction of the intrinsic Mg II emission escape in the galaxy. In subsection 5.2 we dust correct the Mg II escape fractions to estimate the LyC escape fractions. The regions with low Mg II escape, due to the strong correlation between Mg II and dust, have even lower LyC escape fractions (Table 4).

We find that the Integrated aperture, which contains all of the signal from the galaxy, represents the average Mg II and LyC escape fractions of the spatially distinct apertures (Table 4). The central aperture is the brightest region and thus the region where the LyC was observed. The LyC escape fraction from this region is an order of magnitude higher than the inferred average for the spatially integrated area of the galaxy. This places the average of the galaxy below the typically-quoted value needed to reionize the universe even though the central value is above this limit. The variability in the values of each sightline could introduce scatter in the indirect estimators of LyC escape. With this information, we determine that single-sightline observations may not accurately reflect the volume averaged LyC escape fraction. To resolve this issue, an extremely large sample size will provide many different sightline combinations. Combining a large sample size with observations on the scale of our Integrated aperture should reduce scatter and indirectly offer volume averaged escape fractions. The recently launched *James Webb Space Telescope* (JWST) will offer observations of Mg II, which has been redshifted into the IR for high-redshift galaxies. The size of these high-redshift galaxies on the sky means that they fall nicely within one microshutter assembly (MSA). Thus, at high redshifts the JWST will largely probe entire galaxies, as was done with our Integrated aperture, which can reduce the scatter introduced by single sightlines.

## ACKNOWLEDGEMENTS

We would like to acknowledge that the HET is built on Indigenous land. Moreover, we would like to acknowledge and pay our respects to the Carrizo & Comecrudo, Coahuiltecan, Caddo, Tonkawa, Comanche, Lipan Apache, Alabama-Coushatta, Kickapoo, Tigua Pueblo, and all the American Indian and Indigenous Peoples and communities who have been or have become a part of these lands and territories in Texas, here on Turtle Island.

The Hobby-Eberly Telescope (HET) is a joint project of the University of Texas at Austin, the Pennsylvania State University, Ludwig-Maximilians-Universität München, and Georg-August-Universität Göttingen. The HET is named in honor of its principal benefactors, William P. Hobby and Robert E. Eberly.

The Low Resolution Spectrograph 2 (LRS2) was developed and funded by the University of Texas at Austin McDonald Observatory and Department of Astronomy and by Pennsylvania State University. We thank the Leibniz-Institut für Astrophysik Potsdam (AIP) and the Institut für Astrophysik Göttingen (IAG) for their contributions to the construction of the integral field units.

## DATA AVAILABILITY

The data underlying this article will be shared on request to the corresponding author.

## REFERENCES

- Aguado D. S., et al., 2019, *ApJS*, **240**, 23
- Astropy Collaboration et al., 2018, *AJ*, **156**, 123
- Bañados E., et al., 2017, *Nature*, **553**, 473–476
- Becker R. H., et al., 2001, *The Astronomical Journal*, **122**, 2850
- Becker G. D., D’Aloisio A., Christenson H. M., Zhu Y., Worseck G., Bolton J. S., 2021, *MNRAS*, **508**, 1853
- Berg D. A., 2013, PhD thesis, University of Minnesota, United States
- Borthakur S., Heckman T. M., Leitherer C., Overzier R. A., 2014, *Science*, **346**, 216
- Bullock J. S., Kravtsov A. V., Weinberg D. H., 2000, *ApJ*, **539**, 517
- Cardelli J. A., Clayton G. C., Mathis J. S., 1989, *ApJ*, **345**, 245
- Chisholm J., et al., 2018, *Astronomy & Astrophysics*, **616**, A30
- Chisholm J., Prochaska J. X., Schaerer D., Gazagnes S., Henry A., 2020, *MNRAS*, **498**, 2554
- Chonis T. S., Hill G. J., Lee H., Tuttle S. E., Vattiat B. L., 2014, *Ground-based and Airborne Instrumentation for Astronomy V*
- Fan X., et al., 2006, *The Astronomical Journal*, **132**, 117
- Faucher-Giguère C.-A., Lidz A., Zaldarriaga M., Hernquist L., 2009, *The Astrophysical Journal*, **703**, 1416–1443
- Finkelstein S. L., et al., 2019, *The Astrophysical Journal*, **879**, 36
- Fletcher T. J., Tang M., Robertson B. E., Nakajima K., Ellis R. S., Stark D. P., Inoue A., 2019, *The Astrophysical Journal*, **878**, 87
- Garnett D. R., 1992, *AJ*, **103**, 1330
- Gazagnes S., Chisholm J., Schaerer D., Verhamme A., Rigby J. R., Bayliss M., 2018, *Astronomy & Astrophysics*, **616**, A29
- Gazagnes S., Koopmans L. V. E., Wilkinson M. H. F., 2021, *Monthly Notices of the Royal Astronomical Society*, **502**, 1816–1842
- González Delgado R. M., Leitherer C., Heckman T. M., 1999, *ApJS*, **125**, 489
- Green G. M., Schlafly E., Zucker C., Speagle J. S., Finkbeiner D., 2019, *The Astrophysical Journal*, **887**, 93
- Grimes J. P., et al., 2009, *The Astrophysical Journal Supplement Series*, **181**, 272
- Harris C. R., et al., 2020, *Nature*, **585**, 357
- Henry A., Berg D. A., Scarlata C., Verhamme A., Erb D., 2018, *The Astrophysical Journal*, **855**, 96
- Hopkins P. F., Hernquist L., Cox T. J., Kereš D., 2008, *The Astrophysical Journal Supplement Series*, **175**, 356–389
- Izotov Y. I., Schaerer D., Thuan T. X., Worseck G., Guseva N. G., Orlitová I., Verhamme A., 2016a, *Monthly Notices of the Royal Astronomical Society*, **461**, 3683
- Izotov Y. I., Orlitová I., Schaerer D., Thuan T. X., Verhamme A., Guseva N. G., Worseck G., 2016b, *Nature*, **529**, 178–180
- Izotov Y. I., Schaerer D., Worseck G., Guseva N. G., Thuan T. X., Verhamme A., Orlitová I., Fricke K. J., 2017, *Monthly Notices of the Royal Astronomical Society*, **474**, 4514
- Izotov Y. I., Worseck G., Schaerer D., Guseva N. G., Thuan T. X., Fricke Verhamme A., Orlitová I., 2018, *Monthly Notices of the Royal Astronomical Society*, **478**, 4851
- Izotov Y. I., Worseck G., Schaerer D., Guseva N. G., Chisholm J., Thuan T. X., Fricke K. J., Verhamme A., 2021, *Monthly Notices of the Royal Astronomical Society*, **503**, 1734–1752
- Kramida A., Yu. Ralchenko Reader J., and NIST ASD Team 2021, NIST Atomic Spectra Database (ver. 5.9), [Online]. Available: <https://physics.nist.gov/asd> [2017, April 9]. National Institute of Standards and Technology, Gaithersburg, MD.
- Leitet, E. Bergvall, N. Piskunov, N. Andersson, B.-G. 2011, *A&A*, **532**, A107
- Leitherer C., Hernandez S., Lee J. C., Oey M. S., 2016, *The Astrophysical Journal*, **823**, 64

- Luridiana V., Morisset C., Shaw R. A., 2014, *Astronomy & Astrophysics*, 573, A42
- Madau P., Dickinson M., 2014, *Annual Review of Astronomy and Astrophysics*, 52, 415–486
- Madau P., Haardt F., 2015, *The Astrophysical Journal*, 813, L8
- Matsuoka Y., et al., 2018, *The Astrophysical Journal*, 869, 150
- Matthee J., et al., 2021, (Re)Solving Reionization with Ly $\alpha$  : *How Bright Ly $\alpha$  Emitters account for the  $z \approx 2 - 8$  Cosmic Ionizing Background* ([arXiv:2110.11967](https://arxiv.org/abs/2110.11967))
- Miralda-Escudé J., Rees M. J., 1994, *MNRAS*, 266, 343
- Naidu R. P., Forrest B., Oesch P. A., Tran K.-V. H., Holden B. P., 2018, *MNRAS*, 478, 791
- Naidu R. P., Tacchella S., Mason C. A., Bose S., Oesch P. A., Conroy C., 2020, *The Astrophysical Journal*, 892, 109
- Nakajima K., Ouchi M., 2014, *Monthly Notices of the Royal Astronomical Society*, 442, 900–916
- Newville M., Stensitzki T., Allen D. B., Ingargiola A., 2014, LMFIT: Non-Linear Least-Square Minimization and Curve-Fitting for Python, [doi:10.5281/zenodo.11813](https://doi.org/10.5281/zenodo.11813), <https://doi.org/10.5281/zenodo.11813>
- Oesch P. A., et al., 2009, *The Astrophysical Journal*, 709, L16–L20
- Oey M. S., Pellegrini E. W., Zastrow J., Jaskot A. E., 2014, Ionization by Massive Young Clusters as Revealed by Ionization-Parameter Mapping ([arXiv:1401.5779](https://arxiv.org/abs/1401.5779))
- Onoue M., et al., 2017, *The Astrophysical Journal*, 847, L15
- Osterbrock D. E., 1989, *Astrophysics of gaseous nebulae and active galactic nuclei*
- Planck Collaboration et al., 2021, *A&A*, 652, C4
- Reddy N. A., Steidel C. C., Pettini M., Bogosavljević M., 2016, *ApJ*, 828, 107
- Ricci F., Marchesi S., Shankar F., La Franca F., Civano F., 2016, *Monthly Notices of the Royal Astronomical Society*, 465, 1915
- Rivera-Thorsen T. E., et al., 2017, *Astronomy & Astrophysics*, 608, L4
- Rivera-Thorsen T. E., et al., 2019, *Science*, 366, 738
- Robertson B. E., et al., 2013, *The Astrophysical Journal*, 768, 71
- Robertson B. E., Ellis R. S., Furlanetto S. R., Dunlop J. S., 2015, *The Astrophysical Journal*, 802, L19
- Rosa-González D., Terlevich E., Terlevich R., 2002, *Monthly Notices of the Royal Astronomical Society*, 332, 283–295
- Shapley A. E., Steidel C. C., Strom A. L., Bogosavljević M., Reddy N. A., Siana B., Mostardi R. E., Rudie G. C., 2016, *The Astrophysical Journal*, 826, L24
- Shen X., Hopkins P. F., Faucher-Giguère C.-A., Alexander D. M., Richards G. T., Ross N. P., Hickox R. C., 2020, *Monthly Notices of the Royal Astronomical Society*, 495, 3252
- Smee S. A., et al., 2013, *The Astronomical Journal*, 146, 32
- Steidel C. C., Bogosavljević M., Shapley A. E., Reddy N. A., Rudie G. C., Pettini M., Trainor R. F., Strom A. L., 2018, *The Astrophysical Journal*, 869, 123
- Vanzella E., et al., 2010, *The Astrophysical Journal*, 725, 1011
- Vanzella E., et al., 2016, *The Astrophysical Journal*, 825, 41
- Verhamme A., Orlitová I., Schaerer D., Hayes M., 2015, *Astronomy & Astrophysics*, 578, A7
- Wang T., et al., 2019, *Nature*, 572, 211–214
- Witstok J., Smit R., Maiolino R., Curti M., Laporte N., Massey R., Richard J., Swinbank M., 2021, *Monthly Notices of the Royal Astronomical Society*, 508, 1686–1700

This paper has been typeset from a  $\text{\LaTeX}$  file prepared by the author.